

# Advances in Sensitivity Encoding With Arbitrary $k$ -Space Trajectories

Klaas P. Pruessmann,<sup>1</sup> Markus Weiger,<sup>1</sup> Peter Börnert,<sup>2</sup> and Peter Boesiger<sup>1\*</sup>

**New, efficient reconstruction procedures are proposed for sensitivity encoding (SENSE) with arbitrary  $k$ -space trajectories. The presented methods combine gridding principles with so-called conjugate-gradient iteration. In this fashion, the bulk of the work of reconstruction can be performed by fast Fourier transform (FFT), reducing the complexity of data processing to the same order of magnitude as in conventional gridding reconstruction. Using the proposed method, SENSE becomes practical with non-standard  $k$ -space trajectories, enabling considerable scan time reduction with respect to mere gradient encoding. This is illustrated by imaging simulations with spiral, radial, and random  $k$ -space patterns. Simulations were also used for investigating the convergence behavior of the proposed algorithm and its dependence on the factor by which gradient encoding is reduced. The in vivo feasibility of non-Cartesian SENSE imaging with iterative reconstruction is demonstrated by examples of brain and cardiac imaging using spiral trajectories. In brain imaging with six receiver coils, the number of spiral interleaves was reduced by factors ranging from 2 to 6. In cardiac real-time imaging with four coils, spiral SENSE permitted reducing the scan time per image from 112 ms to 56 ms, thus doubling the frame-rate. Magn Reson Med 46:638–651, 2001. © 2001 Wiley-Liss, Inc.**

**Key words:** sensitivity encoding; SENSE;  $k$ -space trajectories; spiral imaging; iterative reconstruction

Arrays of simultaneously operated receiver coils have recently attracted increasing attention as a means of enhancing scan speed in MRI. Several authors have proposed imaging schemes designed to utilize parallel signal acquisition with multiple coils for the purpose of reducing scan time (1–8). Exploiting knowledge of spatial coil sensitivity, these techniques enable the reduction of the number of gradient-encoding steps without compromising spatial resolution or the field of view (FOV).

Due to the specific role of coil sensitivity, array imaging with reduced  $k$ -space sampling requires particular considerations for image generation. As coil sensitivity is used as a means of signal encoding, the net encoding functions are no longer harmonics of the FOV as in conventional Fourier imaging. Consequently, image reconstruction from under-sampled multiple-coil data cannot be performed by mere Fourier transform (FT) but requires specialized processing.

A general approach to the reconstruction problem was described in Ref. 6, introducing the SENSitivity Encoding

(SENSE) method. In this work, reconstruction formulae were derived for array imaging with arbitrary coil configurations and  $k$ -space trajectories. However, in their general form these formulae are numerically rather demanding.

An efficient implementation was previously described for the special case of sampling  $k$ -space along a regular Cartesian grid (6). In this case, SENSE processing may be performed in a fashion similar to earlier Cartesian approaches (2,4). In a first step, conventional Fourier reconstruction is performed for each coil element, yielding a set of aliased images with reduced FOV. In a second step, the aliasing is undone using knowledge of the individual coil sensitivities. This latter step requires little computation because the aliasing effect superimposes the signal of only a small number of volume elements in each pixel of the reduced FOV. In other words, the point spread function (PSF), which corresponds to Cartesian undersampling, is well behaved in that it exhibits sharply localized, equidistant peaks.

With general  $k$ -space trajectories, such as spirals (9,10) or radial (11,12) and stochastic (13) schemes, the situation is more complicated. Similarly to the Cartesian case, SENSE permits reducing the density of general sampling patterns while maintaining the covered  $k$ -space area. However, arbitrary  $k$ -space patterns entail highly variable PSFs. With spiral acquisition, for example, the PSF exhibits continuous, ring-shaped structures rather than evenly spaced, isolated peaks (14). As a consequence, the aliasing that results from reducing  $k$ -space density is considerably more complex and prevents straightforward unfolding in the image domain. This observation illustrates why general SENSE reconstruction has so far been seriously hampered by its numerical complexity (15).

In this work we propose a novel, highly efficient implementation of non-Cartesian SENSE processing. The new approach is based on the idea of performing reconstruction iteratively, as recently proposed independently by the authors and by Kannengießer et al. (16,17). It is shown that so-called *weak* reconstruction with SNR optimization can be accomplished using the conjugate-gradient (CG) iteration method (18). **The key improvement in reconstruction speed is then achieved by combining fast Fourier transform (FFT) with forward and reverse gridding operations for efficient execution of the CG iteration loops.** Further speed benefits are accomplished by several measures of preconditioning and numerical optimization.

Using the proposed procedure, the computation times required for non-Cartesian SENSE reconstruction are considerably diminished, making sensitivity-encoded imaging practical with arbitrary acquisition patterns. The general applicability of the method has been verified by imaging simulations with spiral, radial, and random trajectories, as well as Cartesian sampling for comparison. The in vivo feasibility of the new approach is demon-

<sup>1</sup>Institute of Biomedical Engineering, University of Zürich and Swiss Federal Institute of Technology Zürich, Switzerland.

<sup>2</sup>Philips Research Laboratory Hamburg, Division Technical Systems, Hamburg, Germany.

Grant sponsor: EUREKA; Grant number: EU1353; Grant sponsor: KTI; Grant number: 3030.2.

\*Correspondence to: Dr. P. Boesiger, Institute of Biomedical Engineering, University of Zürich and ETH Zürich, Gloriastrasse 35, CH-8092 Zürich, Switzerland.

Received 22 November 2000; revised 17 January 2001; accepted 5 February 2001.

2001 ISMRM Young Investigator I.I. Rabi Award Finalist.

© 2001 Wiley-Liss, Inc.

strated by examples of spiral SENSE imaging of the brain and heart.

## THEORY AND METHODS

### Reconstruction Problem

The problem of sensitivity-based image reconstruction from multiple-coil data, obtained with general  $k$ -space trajectories, was previously studied theoretically in Ref. 6. The concepts proposed in that work were based on considerations of voxel functions, reflecting the spatial signal response associated with pixel values. Two strategies for ensuring suitable voxel functions, both characterized by underlying voxel conditions, were suggested. The first approach strictly requires the resulting voxel functions to be best approximations of given prototypes, e.g., box or Dirac shapes. The second approach uses a weaker voxel condition, requiring only that the resulting voxel functions share the orthogonality relations of their ideal counterparts.

This latter approach forms the basis of the present work. Following the notation used in Ref. 6, the weak voxel condition reads:

$$FE = Id \quad [1]$$

where  $E$  and  $F$  denote the encoding and reconstruction matrices, respectively, and  $Id$  denotes the identity matrix. The reconstruction matrix  $F$  represents the linear mapping of sample values used for creating the desired image. The encoding matrix  $E$  is formed by the scalar products of the hybrid gradient and sensitivity encoding functions and the chosen voxel prototypes. In the scope of this work, Dirac distributions are used as voxel prototypes, forming a regular Cartesian grid corresponding to a common  $N \times N$  image matrix. With the Dirac choice, the weak voxel condition may be restated more intuitively as: each voxel function must be equal to 1 in the center of the voxel to which it belongs, and equal to zero in all other voxels' centers. The entries of the encoding matrix then reduce to

$$E_{(\gamma,\kappa),\rho} = e^{ik_\kappa r_\rho} s_\gamma(\mathbf{r}_\rho), \quad [2]$$

where  $\mathbf{r}_\rho$  denotes the position of the  $\rho$ -th voxel,  $\mathbf{k}_\kappa$  the  $\kappa$ -th sampling position in  $k$ -space, and  $s_\gamma$  the complex spatial sensitivity of the  $\gamma$ -th coil.

Let  $n_C$  and  $n_K$  denote the number of receiver coils used and the number of sampling positions in  $k$ -space, respectively. Often the total number of encoding functions,  $n_C n_K$ , exceeds  $N^2$ . Then Eq. [1] is underdetermined, leaving degrees of freedom in the choice of the reconstruction matrix, which may be exploited for optimizing SNR. As derived in Ref. 6, in terms of SNR the best solution of Eq. [1] is given by

$$F = (E^H \tilde{\Psi}^{-1} E)^{-1} E^H \tilde{\Psi}^{-1}, \quad [3]$$

where the superscript  $H$  indicates the complex conjugate transpose, and  $\tilde{\Psi}$  denotes the sample noise matrix, which describes the levels and the correlation of stochastic noise

in signal samples. Using this expression for the reconstruction matrix, image reconstruction is performed by:

$$\mathbf{v} = (E^H \tilde{\Psi}^{-1} E)^{-1} E^H \tilde{\Psi}^{-1} \mathbf{m}, \quad [4]$$

where  $\mathbf{m}$  and  $\mathbf{v}$  are vectors of length  $n_C n_K$  and  $N^2$ , respectively, listing the complex sample values acquired and the complex pixel values of the reconstructed image. Stochastic noise in the final image is described by the image noise matrix:

$$X = F \tilde{\Psi} F^H = (E^H \tilde{\Psi}^{-1} E)^{-1}. \quad [5]$$

For efficient numerical evaluation, Eq. [4] is rewritten as a linear system of equations with the unknown image vector  $\mathbf{v}$ :

$$(E^H \tilde{\Psi}^{-1} E) \mathbf{v} = E^H \tilde{\Psi}^{-1} \mathbf{m}. \quad [6]$$

### Iterative Solving

Solving the system described by Eq. [6] is numerically challenging, as it is usually rather large. The size of  $E$  is  $n_C n_K \times N^2$ , and the matrix in brackets has size  $N^2 \times N^2$ . Handling these matrices in a straightforward manner requires large amounts of memory and processing time. In particular, using direct methods for solving the equation entails massive computation with a number of operations on the order of  $N^6$ . Calculating a  $128 \times 128$  image, e.g., would require more than  $10^{12}$  operations and about 1 GB of memory, making image reconstruction rather tedious with present-day workstations.

One key to more efficient processing is solving Eq. [6] iteratively. Starting with some initial vector, iterative algorithms yield a progression of approximate solutions, which converge to the exact solution. A variety of such techniques exist for the treatment of large linear systems. For the present case, the so-called conjugate-gradient (CG) method (18) is particularly suited. On the one hand, as shown later in this section, it may be combined with FFT for very efficient calculations. On the other hand, the CG iteration does not require particular provisions for ensuring convergence. It converges safely given that the coefficient matrix involved is positive definite, which holds for the system described by Eq. [6] (see Appendix A).

The CG algorithm theoretically yields the exact solution of an  $N^2 \times N^2$  system after at most  $N^2$  iterations. For  $N$  in the range of 128, though, it is not practical to carry out the entire procedure. However, for well-behaved problems, sufficiently accurate approximations are obtained after a relatively small number of iterations (19).

Each CG iteration step consists in multiplying the matrix to be inverted with a residuum vector and several further calculations of minor complexity. Thus the iteration speed depends crucially on how fast matrix-vector multiplication can be performed. The number of iterations necessary to achieve a given accuracy is related to the so-called *condition* of the matrix to be inverted and the suitability of the starting vector. Fortunately, in the present case, these factors can be greatly influenced by several measures of numerical optimization, as discussed in the following.

### Elimination of the Noise Matrix

In a first step, Eq. [6] is simplified by eliminating the sample noise matrix. Note that noise levels and correlation are considered exclusively for the sake of minimizing noise in the final image. The correct spatial assignment of the MR signal is independently ensured by the voxel condition in Eq. [1], which is fulfilled also if the noise statistics are not correctly taken into account. This can be easily verified by inserting Eq. [3] into Eq. [1].

Hence, one option for eliminating the noise matrix is to skip noise assessment and simply replace  $\tilde{\Psi}$  by identity. As a result, noise in the final image will not be exactly minimized. The severity of this drawback is difficult to estimate a priori without actually calculating image noise. Generally, the benefit of considering noise statistics scales with encoding redundancy and is greater the less equivalent the coils are with respect to load, gain, mutual coupling, and electronic noise.

To eliminate the noise matrix from Eq. [6] without compromising the SNR in the final image, it is necessary to consider the structure of  $\tilde{\Psi}$ . This matrix has one row and one column for each hybrid encoding carried out, thus its size is  $n_C n_K \times n_C n_K$ . Each diagonal entry represents the variance of noise in the corresponding sample value, while the off-diagonal elements reflect noise correlation between samples.

Noise correlation occurs mainly between samples taken simultaneously with different coils. On the one hand, coils with overlapping sensitive regions receive partly identical thermal radiation. On the other hand, coil coupling gives rise to mutual noise transmission. To a certain degree, noise correlation does also occur between successive samples acquired with the same coil, especially when oversampling is applied. However, this effect shall be neglected in the scope of this work. Furthermore, it is assumed that noise correlation between different coils is constant over time, as the underlying mechanisms are approximately invariant. Receiver noise is then described by a sparse matrix with a simple structure:

$$\tilde{\Psi}_{(\gamma,\kappa),(\gamma',\kappa')} = \Psi_{\gamma,\gamma'} \delta_{\kappa,\kappa'}. \quad [7]$$

In this formulation, the Kronecker delta symbol expresses the assumption that noise correlation occurs only between samples taken simultaneously at the same position in  $k$ -space. The time-independent  $n_C \times n_C$  matrix  $\Psi$  can be determined experimentally by statistical analysis of reference noise samples taken in the absence of MR signal. Let  $\eta_\gamma$  denote the noise output of the  $\gamma$ -th channel. Then the entries of  $\Psi$  are given by:

$$\Psi_{\gamma,\gamma'} = \overline{\eta_\gamma \eta_{\gamma'}^*}, \quad [8]$$

where the bar indicates time averaging. Note that this formula for the determination of  $\Psi$  is statistically equivalent to Eq. [A9] derived in Ref. 6. Using averaging according to Eq. [8], the relative error in each entry of  $\Psi$  decreases only as the inverse square root of the number of noise samples taken. Thus, for reasonable accuracy a number of noise samples in the range of  $10^3$  is advisable, which can readily be obtained during the common scan preparation

phase. Note that noise correlation, just like coil sensitivity, depends on the particular coil and load configuration. Therefore, it is important to collect noise samples in the actual imaging setup.

With noise statistics simplified according to Eq. [7], the noise variance matrix can be eliminated from Eq. [6] by a simple manipulation. The basic idea is to create a set of virtual receiver channels by linear combination of the original ones, such that the virtual channels exhibit unit noise levels and no mutual noise correlation. As shown in Appendix B, suitable weighting coefficients for this purpose are given by the inverse of the matrix  $L$  obtained by Cholesky decomposition (20) of  $\Psi$ :

$$\Psi = LL^H. \quad [9]$$

Virtual sampling data with decorrelated unit noise are thus obtained from the original samples by

$$m_{\gamma,\kappa}^{decorr} = \sum_{\gamma'} (L^{-1})_{\gamma,\gamma'} m_{\gamma',\kappa}. \quad [10]$$

The net coil sensitivities associated with the virtual channels are given likewise by

$$s_\gamma^{decorr}(\mathbf{r}) = \sum_{\gamma'} (L^{-1})_{\gamma,\gamma'} s_{\gamma'}(\mathbf{r}), \quad [11]$$

leading to the modified encoding matrix

$$E_{(\gamma,\kappa),\rho}^{decorr} = e^{ik_\kappa r_\rho} s_\gamma^{decorr}(\mathbf{r}_\rho). \quad [12]$$

With sample values and sensitivities modified in this fashion, the newly combined channels can be treated exactly like physical ones. The noise variance matrix of the virtual channels is equal to identity and can thus be omitted when Eq. [6] is reformulated for image reconstruction from the modified data. Note that by the transition to virtual channels the solution of Eq. [6] is not altered (see Appendix B). In particular, the optimization of SNR is preserved.

Both options—decorrelation and neglecting noise correlation—lead to the same simplified formula. Dropping the superscript for decorrelation, it reads in both cases:

$$(E^H E) \mathbf{v} = E^H \mathbf{m}. \quad [13]$$

### FT for Matrix-Vector Multiplication

In each CG loop, the matrices  $E$  and  $E^H$ , which appear on the left side of Eq. [13], need to be multiplied with some temporary vectors, say,  $\mathbf{x}$  and  $\mathbf{y}$ , respectively. For performing these operations efficiently, advantage is taken of the fact that, despite the sensitivity contribution to hybrid encoding,  $E$  is still characterized by Fourier terms. The  $(\gamma,\kappa)$ -th component of the product  $E\mathbf{x}$ , reads:

$$(E\mathbf{x})_{(\gamma,\kappa)} = \sum_{\rho} e^{ik_\kappa r_\rho} s_\gamma(\mathbf{r}_\rho) x_\rho. \quad [14]$$

The sum on the right may be regarded as the integral of a set of weighted Dirac distributions in the spatial domain

$$(E\mathbf{x})_{(\gamma,\kappa)} = \int e^{ik_{\kappa}r} \sum_{\rho} (s_{\gamma}(\mathbf{r}_{\rho})x_{\rho}\delta(\mathbf{r} - \mathbf{r}_{\rho}))d\mathbf{r}, \quad [15]$$

which is the inverse FT of the distribution set, sampled at  $\mathbf{k}_{\kappa}$ :

$$(E\mathbf{x})_{(\gamma,\kappa)} = FT^{-1} \left[ \sum_{\rho} s_{\gamma}(\mathbf{r}_{\rho})x_{\rho}\delta(\mathbf{r} - \mathbf{r}_{\rho}) \right] (\mathbf{k}_{\kappa}). \quad [16]$$

Similarly, the  $\rho$ -th component of the product of  $E^H$  and  $\mathbf{y}$ ,

$$(E^H\mathbf{y})_{\rho} = \sum_{\gamma,\kappa} e^{-ik_{\kappa}r_{\rho}} s_{\gamma}^*(\mathbf{r}_{\rho})y_{\gamma,\kappa}, \quad [17]$$

can be regarded as a sum of  $k$ -space integrals weighted by complex conjugate coil sensitivity,

$$(E^H\mathbf{y})_{\rho} = \sum_{\gamma} s_{\gamma}^*(\mathbf{r}_{\rho}) \left( \int e^{-ik_{\kappa}r_{\rho}} \sum_{\kappa} (y_{(\gamma,\kappa)}\delta(\mathbf{k} - \mathbf{k}_{\kappa}))d\mathbf{k} \right), \quad [18]$$

where the term in brackets represents a forward FT, sampled at  $\mathbf{r}_{\rho}$ :

$$(E^H\mathbf{y})_{\rho} = \sum_{\gamma} s_{\gamma}^*(\mathbf{r}_{\rho}) \left( FT \left[ \sum_{\kappa} (y_{(\gamma,\kappa)}\delta(\mathbf{k} - \mathbf{k}_{\kappa})) \right] (\mathbf{r}_{\rho}) \right). \quad [19]$$

The FTs in Eqs. [16] and [19] can essentially be calculated by FFT. However, while the voxel positions,  $\mathbf{r}_{\rho}$ , form a regular Cartesian grid compatible with FFT, the  $k$ -space positions,  $\mathbf{k}_{\kappa}$ , form an arbitrary sampling pattern. Therefore, additional gridding is required preceding and following the forward and reverse transforms, respectively. This step can be accomplished by convolution and resampling following the same principles as used for common gridding reconstruction (21). Note that for this operation the experimental trajectory need not fulfill the Nyquist density criterion. Nevertheless, the Cartesian  $k$ -space grid used for resampling must be sufficiently dense in order to avoid aliasing artifact in the calculated FTs. In both directions the FFT and gridding procedure must be repeated for each coil, as the functions to be transformed are coil-dependent.

By applying Eqs. [16] and [19] successively, the matrix-vector multiplications required for iterative solving of Eq. [13] can be performed very efficiently. Indeed, the FFT approach reduces the complexity of a single iteration step drastically from  $O(N) = N^4$  to  $O(N) = N^2 \log N$ . Note also that when using FFT for evaluating  $E^H E\mathbf{x}$ , the matrix  $E$  need not be explicitly calculated or stored.

#### Density and Intensity Correction

A common way of reducing the number of iterations required in the CG method is so-called preconditioning (19). The basic idea of preconditioning is to manipulate the system of equations such that the right side approximates the solution of the system. The right side of Eq. [13] is obtained by multiplication of  $E^H$  with the vector  $\mathbf{m}$  of sample values. According to Eq. [19], this operation is

somewhat similar to conventional processing of non-Cartesian, multiple-coil data. For each coil element an intermediate image is created by gridding and FT (21), followed by sensitivity-weighted summation (22).

Thus, the right side of Eq. [13] represents a rudimentary image reconstruction. Clearly, upon reduced gradient encoding, the resulting image will exhibit aliasing artifact due to the violation of the Nyquist criterion by each set of single-coil data. Nevertheless, this image forms a first approximation of exact reconstruction. Hence, the present problem is a priori favorably conditioned. However, unlike standard gridding, Eq. [19] does not involve any correction for inhomogeneous  $k$ -space density. Furthermore, in the image domain this equation does not imply what is commonly referred to as intensity correction, i.e., the compensation for inhomogeneity of overall coil sensitivity. In the following it is shown how these known correction mechanisms can be incorporated into Eq. [13] for improved preconditioning.

Density correction of the sample vector  $\mathbf{m}$  is performed by the diagonal matrix

$$D_{(\gamma,\kappa),(\gamma,\kappa)} = \frac{1}{d(\mathbf{k}_{\kappa})}, \quad [20]$$

where  $d(\mathbf{k}_{\kappa})$  denotes the relative density of the  $k$ -space sampling pattern at the position  $\mathbf{k}_{\kappa}$ . Unfortunately, this matrix cannot be inserted into Eq. [13] in a straightforward manner, as any manipulation must be performed equally on both sides of the equation. Instead, the following formulation is used:

$$(E^H D E)\mathbf{v} = E^H D \mathbf{m}. \quad [21]$$

This modification does not represent an exact transform. However, note that the matrix  $D$  was put into the same places where earlier the noise matrix appeared. As stated previously, any invertible matrix can replace the noise matrix without violating the voxel condition, although it affects SNR. In fact, the introduction of  $D$  is equivalent to pretending that the noise level in sample values increases linearly with  $k$ -space density, thus misleading SNR optimization to a certain degree.

SNR optimization is based on encoding redundancy, i.e., on the fact that parts of information required for spatial resolution may be available more than just once, be it from different coils or from neighboring positions in  $k$ -space. In such cases the best way to average redundant information depends on the levels and correlation of the concomitant noise. On the one hand, the introduction of density correction in Eq. [21] does not change the relative estimation of noise between coils, but only between  $k$ -space positions. On the other hand, noise relations between closely neighboring positions in  $k$ -space are not changed significantly unless the density function  $d(\mathbf{k}_{\kappa})$  exhibits considerable local changes. Therefore, the SNR drawback of density correction is expected to be negligible with regular types of trajectories, such as spirals and radial patterns, yet may be considerable with, e.g., random sampling.



Note that, as opposed to the noise matrix, which was eliminated for the sake of numerical optimization, the density correction matrix  $D$  is diagonal and therefore causes only minimal extra computation.

The incorporation of intensity correction is relatively simple, as it can be accomplished by exact transforms. According to Eq. [19], the image  $E^H D \mathbf{m}$  is weighted by the sum-of-squares of coil sensitivities. Let  $I$  denote an  $N^2 \times N^2$  diagonal matrix given by the inverse square-root of this weighting factor:

$$I_{p,p} = \frac{1}{\sqrt{\sum_{\gamma} |s_{\gamma}(\mathbf{r}_p)|^2}}. \quad [22]$$

Left-multiplication of Eq. [21] with  $I^2$  yields

$$(I^2 E^H D E) \mathbf{v} = I^2 E^H D \mathbf{m}. \quad [23]$$

In this formulation, the nonaliased components of the image on the right side are intensity-corrected. However, the matrix in brackets is no longer safely positive-definite, as required for using the CG method. To restore this property, the equation is left-multiplied by  $I^{-1}$ , and on the left side the identity  $I I^{-1}$  is inserted:

$$(I E^H D E I)(I^{-1} \mathbf{v}) = I E^H D \mathbf{m}. \quad [24]$$

Note that by this operation the right side and the intermediate solution in brackets were both modified in the same way, i.e., left-multiplied by  $I^{-1}$ . Therefore, the right side still represents a good approximation, corresponding to favorable conditioning, while the leftmost matrix in brackets is now positive-definite (see Appendix A).

Using Eq. [24], both density and intensity correction can be applied in CG iteration. Both correction methods are optional and work independently. For switching either mechanism off, the respective matrix is simply replaced by identity.

### Starting Image

Generally, for fast convergence the starting image of the CG iteration should be a good approximation of the exact solution. However, with preconditioning, as discussed previously, the best choice is simply a zero image. This is because the approximation resulting from the first loop then is a suitably scaled copy of the right side of the system. In this fashion, the iteration is essentially started with the known approximate solution, yet without the need to consider its scaling, which involves numerous factors, including  $N$ ,  $n_C$ ,  $n_K$ , and the units chosen for coil sensitivity and  $k$ -space density.

### Implementation

According to the previous considerations, image reconstruction consists of essentially three steps. First, the right side of Eq. [24] is calculated:

$$\mathbf{a} = I E^H D \mathbf{m}, \quad [25]$$

yielding the intermediate image  $\mathbf{a}$ . In the second step, an approximate solution  $\mathbf{b}_{approx}$  of

$$(I E^H D E I) \mathbf{b} = \mathbf{a} \quad [26]$$

is determined by CG iteration. An approximate solution of Eq. [13] is then obtained by intensity correction of  $\mathbf{b}_{approx}$ :

$$\mathbf{v}_{approx} = I \mathbf{b}_{approx}. \quad [27]$$

Figure 1 schematically shows the implementation of this procedure as used for the present work. Its central part is a CG unit, which controls the iteration process and performs minor calculations required by the CG scheme.

The CG algorithm used is formally described in Appendix C. In each iteration step, it requires the multiplication of the matrix  $I E^H D E I$  with a vector residuum resulting from the previous iteration. This multiplication is carried out by the loop which forms the major part of Fig. 1. First, the current residuum is multiplied by  $I$ . The second step is the application of  $E$ , consisting of coil-wise multiplication by coil sensitivity, followed by individual FFT and gridding along the experimental  $k$ -space trajectory. The transform and gridding steps are jointly represented as FT2. In  $k$ -space, density correction is carried out independently for each channel. The following application of  $E^H$  consists of coil-wise gridding along the Cartesian grid and FFT back to image domain (FT1), followed by individual weighting by complex conjugate coil sensitivity and subsequent summation of the single-coil results. Finally, the sum is again multiplied by  $I$  and then fed back into the CG unit.

For the initial calculation of  $\mathbf{a}$ , advantage is taken of the fact that the matrices applied to the sample vector  $\mathbf{m}$  in Eq. [25] are identical to the leftmost three matrices in Eq. [26]. The sample data obtained from the receiver channels are fed into the corresponding  $k$ -space paths, before density correction. The resulting image  $\mathbf{a}$  is used for initializing the CG unit, which starts the iteration process with  $\mathbf{b}_{approx}^{(0)} = \mathbf{0}$ .

Each iteration loop results in a refined approximation  $\mathbf{b}_{approx}^{(i)}$  to the exact solution of Eq. [26]. As soon as the process has converged, the current approximation is output and multiplied by  $I$  to yield the intensity-corrected reconstruction  $\mathbf{v}_{approx}$ .

As the exact solution is not known, the accuracy of a current approximation can only be estimated. One plausible measure of accuracy is the relative violation of Eq. [26]:

$$\delta = \frac{|I E^H D E I \mathbf{b}_{approx} - \mathbf{a}|}{|\mathbf{a}|}, \quad [28]$$

which can be calculated with little effort as a by-product of the CG operations (Appendix C). Here, the brackets  $|\cdot|$  denote the Euclidean vector length. The relative deviation from the exact solution,

$$\Delta = \frac{|I \mathbf{b}_{approx} - \mathbf{v}|}{|\mathbf{v}|}, \quad [29]$$

is interesting for studies of convergence behavior, yet requires either knowledge of the exact solution  $\mathbf{v}$  or of a

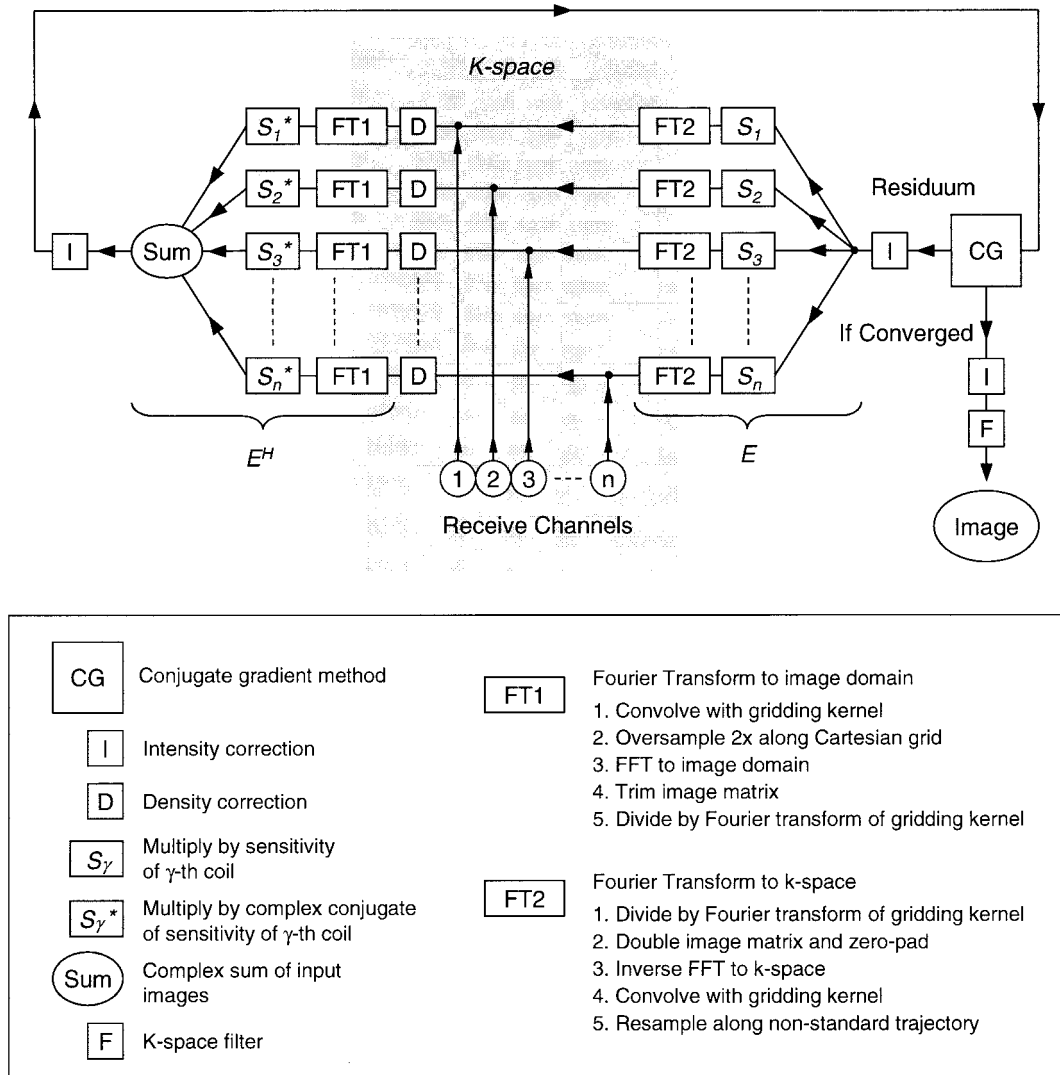


FIG. 1. Implementation of iterative image reconstruction. Conjugate gradient (CG) iteration is controlled by the central CG process. It is initialized by MR data originating from  $N$  receiver channels (1, 2, 3, ...,  $N$ ), acquired with an arbitrary  $k$ -space trajectory. Separately for each channel, these data undergo processing similar to conventional gridding reconstruction, i.e., sampling density correction (D), and resampling along a Cartesian grid, followed by FFT (FT1). The resulting images are individually multiplied by complex conjugate coil sensitivity ( $S_\gamma^*$ ) and summed. After subsequent intensity correction (I), the sum image represents the vector  $\mathbf{a}$  as defined by Eq. [25]. After initialization with  $\mathbf{a}$ , the CG process iteratively calculates a progression of images, which converges towards exact reconstruction. For each iteration step, a current residuum image vector needs to be multiplied by the matrix  $\mathbf{IE}^H \mathbf{DEI}$ . This is performed by the loop which starts from the CG box. After initial intensity correction (I), the processing is continued separately for each receiver coil. First, the intensity corrected residuum image is multiplied by individual coil sensitivity ( $S_\gamma$ ). The results are transformed into  $k$ -space by FFT and resampled along the experimental  $k$ -space trajectory (FT2), resulting in a set of multiple-coil  $k$ -space data similar to that obtained experimentally. The following steps are equivalent to those carried out with the original data, yielding an intermediate image, which is fed back into the CG process. Here a refined approximate solution is calculated, which serves for further refinement by continued iteration. As soon as the current approximation is sufficiently accurate, it is output and undergoes final intensity correction and  $k$ -space filtering.

highly accurate approximation determined by extensive iteration.

#### Gridding

The gridding step included in the module FT1 is equivalent to conventional gridding (21) without density correction. The discrete data along the experimental trajectory  $\mathbf{k}_k$  are convolved with a Kaiser-Bessel kernel and then resampled using a Cartesian grid compatible with FFT. To

suppress gridding artifacts, the Cartesian  $k$ -space grid is chosen so as to yield twice the actual FOV, corresponding to twofold oversampling. After FFT, the resulting image is trimmed to the actual FOV and divided by the FT of the Kaiser-Bessel kernel to compensate for apodization due to the convolution step.

The module FT2 serves for transforming a Cartesian image into  $k$ -space and sampling the transform along the trajectory  $\mathbf{k}_k$ . This is accomplished by the same steps as

used in FT1, yet in reverse order (23). First the image is divided by the FT of the Kaiser-Bessel window. Then the image matrix is extended to twice the FOV, and the added outer regions are padded with zeros. After FFT, the resulting Cartesian  $k$ -space grid is convolved with the Kaiser-Bessel window and resampled along  $\mathbf{k}_c$ .

As in conventional gridding reconstruction, the convolution and resampling steps in both directions are performed discretely using gridding coefficients. These reflect the weights of the input samples in the calculation of interpolated values along the target grid. The coefficients are identical for both gridding directions because of the rotation symmetry of the Kaiser-Bessel window, and must be calculated and stored only once initially.

### $k$ -Space Filtering

As indicated in Fig. 1, the iteratively-found solution of the reconstruction problem requires another final processing step, namely a  $k$ -space filtering operation. This step is necessary when the  $k$ -space trajectory used does not cover the entire, rectangular  $k$ -space region, which corresponds to the desired Cartesian image grid. Spirals and radial patterns, for example, usually have a circular support, and thus do not yield immediate information from the corners of  $k$ -space.

In these cases, SENSE reconstruction is still well defined; that is, the described iterative procedure yields a solution, which includes information about the  $k$ -space corners. This surprising ability is due to the fact that the coil sensitivities have nonfinite Fourier representations, which permit collecting information also from regions away from the actual  $k$ -space trajectory. However, coil sensitivities usually have only very small components of higher spatial frequency. As a consequence, the calculation of outer- $k$ -space information grows increasingly ill-conditioned as the distance from the originally covered area increases. As a consequence, reconstructed  $k$ -space data off the covered region are dominated by strongly amplified noise, which in the spatial domain affects the entire image.

Therefore, these noisy data are eliminated by a  $k$ -space filter. After inverse FFT, the  $k$ -space representation of the solution  $\mathbf{v}_{approx}$  is multiplied by a function which is basically equal to 1 in the region covered by the  $k$ -space trajectory, and equal to zero elsewhere. However, to preserve a well-mannered PSF, the filter should be symmetric and the cutoff needs to be smoothed to a certain degree. Typically, the edge of the trajectory support should be smoothed over a few multiples of  $k_{max}/N$ , whereas the choice of the specific form of the filter is not critical. In the present work, the following filter was used for spiral and radial scanning:

$$f(\mathbf{k}) = \frac{1}{2} + \frac{1}{\pi} \arctan\left(\beta \frac{k_c - |\mathbf{k}|}{k_c}\right), \quad [30]$$

where  $k_c$  denotes the cutoff radius, and the parameter  $\beta$  was set to 100.

After  $k$ -space filtering, forward FFT yields the final image.

### Simulations

For simulations of sensitivity-encoded imaging with arbitrary  $k$ -space trajectories, artificial MR data were created from a high-resolution phantom image by FFT and regridding along the respective  $k$ -space pattern. To suppress gridding artifacts, the image matrix was initially extended to a fourfold size and zero-padded, corresponding to a fourfold increase in  $k$ -space density after FFT. An array of six circular receiver coils was assumed, surrounding the cylindrical phantom without overlap. The complex sensitivities of these coils were calculated using Biot-Savart's law. White noise was added to the artificial signal, with equal variance in all channels and correlation according to the sensitivity overlap within the phantom. In view of this genuine source of noise correlation, additional coil coupling was neglected in simulations for the sake of simplicity.

All computation for the present work was carried out on a 400 MHz DEC Alpha workstation, using PV Wave (Visual Numerics Inc., Houston, TX).

### Experiments

All imaging experiments were performed at 1.5 T on a Philips Gyroscan ACS-NT15. An array of six surface coils (24) with two circular ( $\varnothing = 20$  cm) and four rectangular ( $10 \text{ cm} \times 20 \text{ cm}$ ) elements was used for transverse brain imaging in a volunteer. The circular coils were placed laterally, the rectangular ones were placed in nonoverlapping pairs in anterior and posterior position, with their long diameters along the body axis. A standard spiral scan with 12 interleaves was used for data acquisition (matrix =  $256 \times 256$ , TE = 2 ms, TR = 2 s, flip angle =  $45^\circ$ , acquisition interval = 30 ms).

The four rectangular elements of the same coil array were also used for sensitivity-encoded cardiac imaging in a volunteer. The coils were placed in pairs in anterior and posterior positions, with their long diameters along the body axis. A conventional real-time spiral protocol was used, acquiring four interleaves per  $128 \times 128$  image (TE = 5 ms, TR = 28 ms, flip angle =  $20^\circ$ , acquisition interval = 17 ms). Spectral-spatial selective excitation was used for suppressing fat signal. The FOV was chosen slightly smaller than the chest size, aided by two lateral rest slabs saturated prior to every fourth repetition.

## RESULTS

### Simulations

Sensitivity-encoded imaging with iterative reconstruction was simulated using four types of  $k$ -space trajectories: spiral, Cartesian, radial, and random. The size of the image matrix was  $256 \times 256$ . The noise level in the six receiver channels was chosen so as to yield a root-mean-square SNR of 25 with full Cartesian sampling and conventional reconstruction.

For sensitivity-encoded Cartesian imaging, the sampling density in  $k$ -space was reduced to 40% with respect to full Fourier encoding by increasing the distance of readout lines. For spiral acquisition, a standard, noninterleaved spiral trajectory with variable angular speed was used (25),

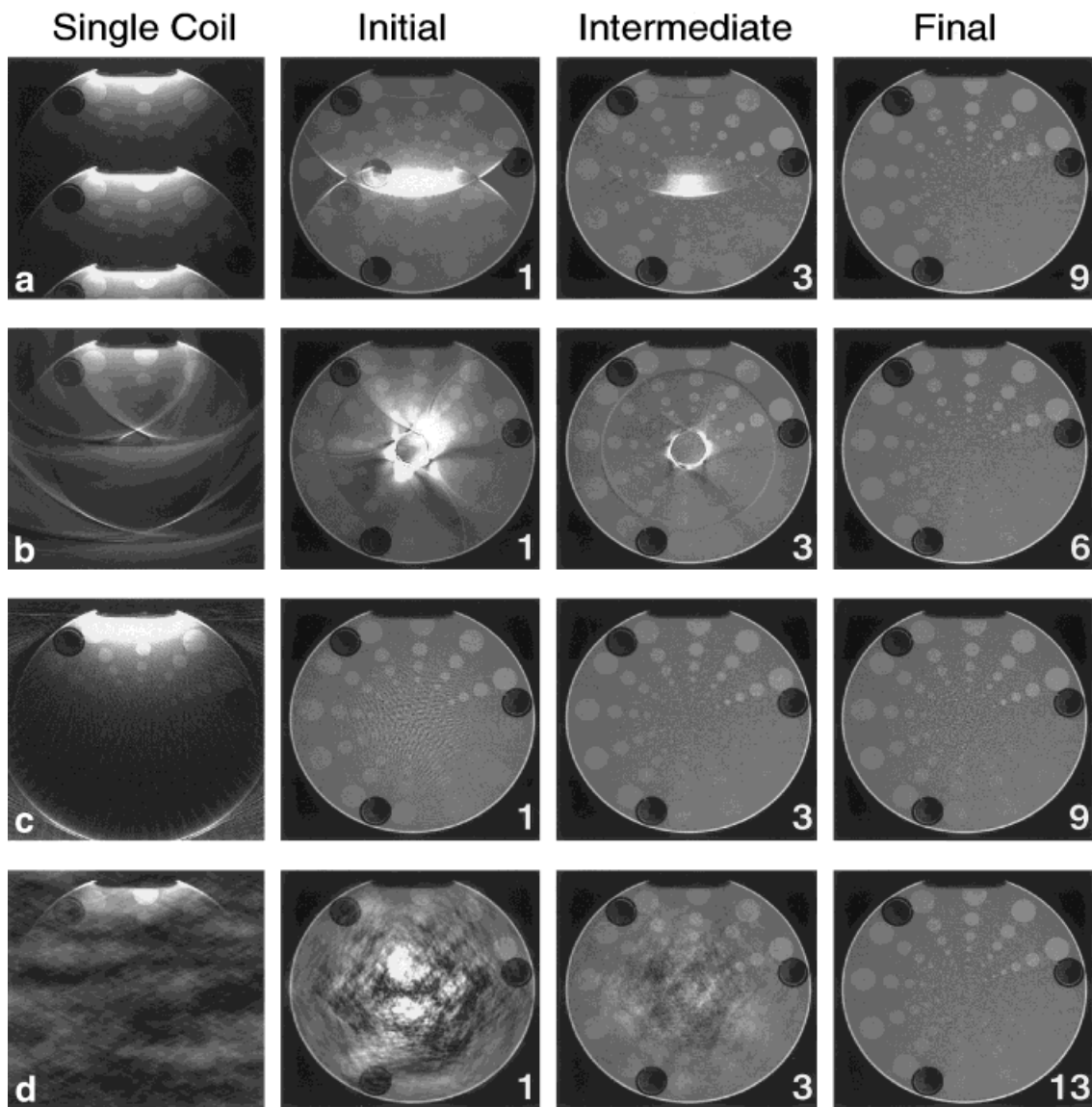


FIG. 2. Simulated sensitivity-encoded imaging with different  $k$ -space sampling patterns. MR data acquisition was simulated with six surface coils placed around a phantom and reduced (a) Cartesian, (b) spiral, (c) radial, and (d) random gradient encoding. The first column shows conventional, single-coil reconstructions, demonstrating the aliasing effect of  $k$ -space undersampling. In the next columns, three stages of iterative image reconstruction are illustrated. The first approximation is shown, followed by an intermediate one, and then by the final image. The numbers indicate the iteration counts.

with the radial spacing of equidistant spiral turns likewise increased by the reduction factor  $R = 2.5$ . The radial sampling pattern was chosen such that its circumferential density was 40% of the Nyquist limit at one-third of the full radius. In the read-out direction the standard sampling densities were maintained with all three trajectory types. For random sampling, the same number of sampling positions as used for reduced Cartesian acquisition were randomly spread within the same part of  $k$ -space.

For reconstruction, both density and intensity correction were used. Between five and 12 iterations were necessary for reducing aliasing artifacts to a negligible level, as illustrated by Fig. 2. For each type of acquisition, this figure shows the first approximation, an intermediate stage, and the final image. For comparison, sample single-

coil images are added, as obtained with conventional gridding reconstruction.

The iteration speed varied slightly among the different trajectories due to the dependence of the gridding effort on the number of  $k$ -space samples. The average computation time per iteration step was 68 s. For comparison, in similar simulations with  $64 \times 64$  and  $128 \times 128$  image matrices, one iteration took an average 4.5 s and 17.5 s, respectively. These numbers reflect the approximately square dependence of the computational cost of gridding and FFT on the image matrix size  $N$ .

In further simulations, the convergence behavior of the proposed method was studied. First, the influence of preconditioning by density and intensity correction was investigated. Spiral acquisition with six coils was simulated



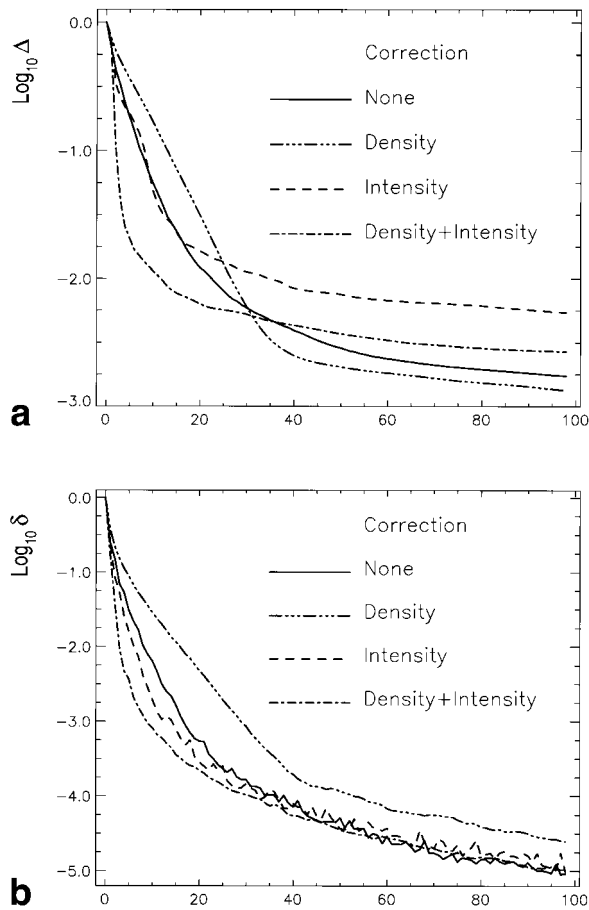


FIG. 3. Effect of preconditioning by density and intensity correction. Logarithmic plots of (a) the true image error  $\Delta$ , and (b) the criterion  $\delta$  as functions of the iteration count in iterative reconstruction from spiral data obtained with  $R = 2.0$ . Different linestyles indicate the type of preconditioning used.

with a  $64 \times 64$  image matrix and radial sampling density reduced to one-half ( $R = 2.0$ ). From the resulting data, a virtually exact reconstruction was calculated as a reference, using 500 iterations without preconditioning. Then iterative reconstruction with 100 iterations was repeated four times with density and intensity correction switched on and off independently. During these four cycles, the convergence towards the exact solution was monitored by means of the two error terms defined in the Methods section (Fig. 3). The plots of the true error,  $\Delta$ , reveal a considerable influence of the correction mechanisms on convergence behavior. The fastest initial convergence was obtained with combined density and intensity correction. Very high accuracy was most rapidly accomplished with density correction alone. By comparison, the readily available second criterion,  $\delta$  (see Eq. [28]), gives a somewhat different picture, reaching significantly higher accuracy values and disguising the relative performance of the correction variants.

A second series of  $64 \times 64$  simulations focused on the influence of the reduction factor  $R$  on convergence speed. Spiral acquisition was simulated with full Fourier encoding ( $R = 1.0$ ) and reduction between  $R = 2.0$  and  $R =$

6.0. Iterative reconstruction using both density and intensity correction showed the convergence behavior plotted in Fig. 4. The true error,  $\Delta$ , reveals a strong dependence of convergence speed on the degree of reduction. As reduction increases, convergence generally slows down. Again, the second criterion,  $\delta$ , suggests faster convergence and understates the influence of the reduction factor.

## Experiments

Using the brain protocol, data sets with reduced gradient encoding were created by selecting between six and two out of 12 interleaves, corresponding to reduction factors between  $R = 2.0$  and  $R = 6.0$ . The reduced sets of interleaves were selected with equidistant starting angles where possible. In the case of five interleaves ( $R = 2.4$ ), the reduced set exhibited both two- and threefold angle increments.

Sensitivity maps were created from a conventional reconstruction including all 12 interleaves and an additional body coil image, using the methods described in Ref. 6. From the reduced data sets, image reconstruction was performed iteratively with density and intensity correction. The iteration was stopped as soon as the image quality was no longer visibly improving. With maximum re-

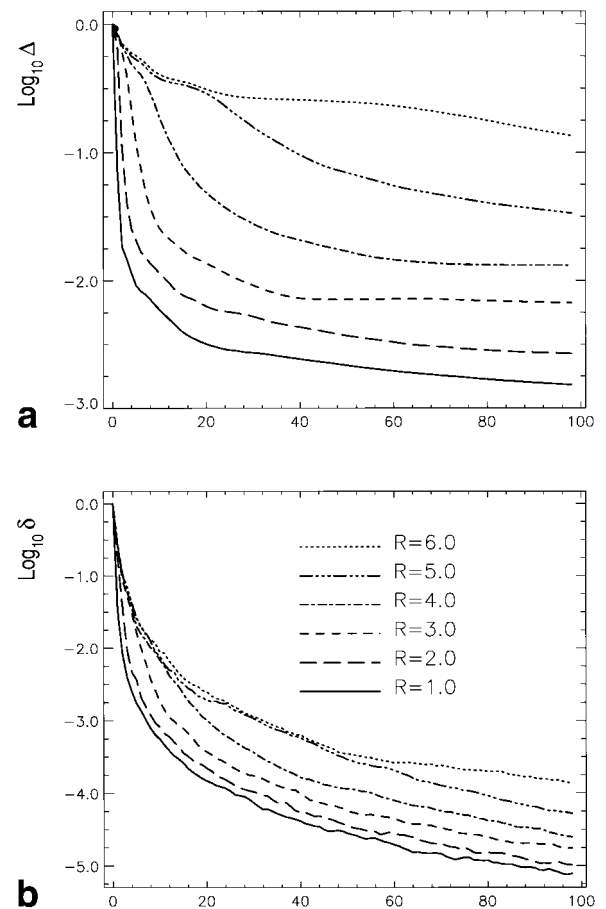


FIG. 4. Convergence speed vs. reduction factor. Logarithmic plots of (a) the true image error  $\Delta$ , and (b) the criterion  $\delta$  as functions of the iteration count in iterative reconstruction. Different linestyles indicate different reduction factors, as indicated in b.

Table 1  
The Number of CG Iterations Required for Image Reconstruction  
as a Function of the SENSE Reduction Factor

Reduction factor $R$	1.0	2.0	2.4	3.0	4.0	6.0
Number of iterations	3	6	10	15	50	99

duction ( $R = 6.0$ ), the process was stopped prematurely after 99 iterations. The number of iterations required are listed in Table 1.

The resulting images are shown in Fig. 5. For full Fourier encoding and each degree of reduction, the intensity-corrected initial and final images of the iteration process are displayed. For comparison, conventionally reconstructed images are added, based on data from only one coil element. The single-coil images show equidistant ring-shaped aliasing as typical for spiral undersampling. Only with  $R = 2.4$ , the aliasing artifacts are less regular due to the varying  $k$ -space distance between the inter-

leaves used. The final images exhibit good quality up to  $R = 3.0$ . Towards fourfold reduction, noise enhancement becomes prominent. The final image obtained with  $R = 6.0$  shows strongly amplified noise and remaining aliasing artifact due to incomplete convergence.

Using the cardiac real-time protocol, data were acquired during several heartbeats in a free-running mode, i.e., without ECG triggering and breath control. The acquisition order in each set of four interleaves was  $0^\circ$ ,  $180^\circ$ ,  $90^\circ$ , and  $270^\circ$ . Thus, the first and second pair of successive interleaves could alternatively be regarded as independent acquisitions with  $R = 2.0$ . The acquisition of each half set took 56 ms, corresponding to 112 ms for full Fourier encoding.

A first series of images was obtained by conventional gridding reconstruction. Using this series as a reference, sensitivity maps were created using the methods described in Refs. 6 and 26. The process included time averaging of raw sensitivity, division by the root-sum-of-squares of the array images, and final correction for net sensitivity fall-off

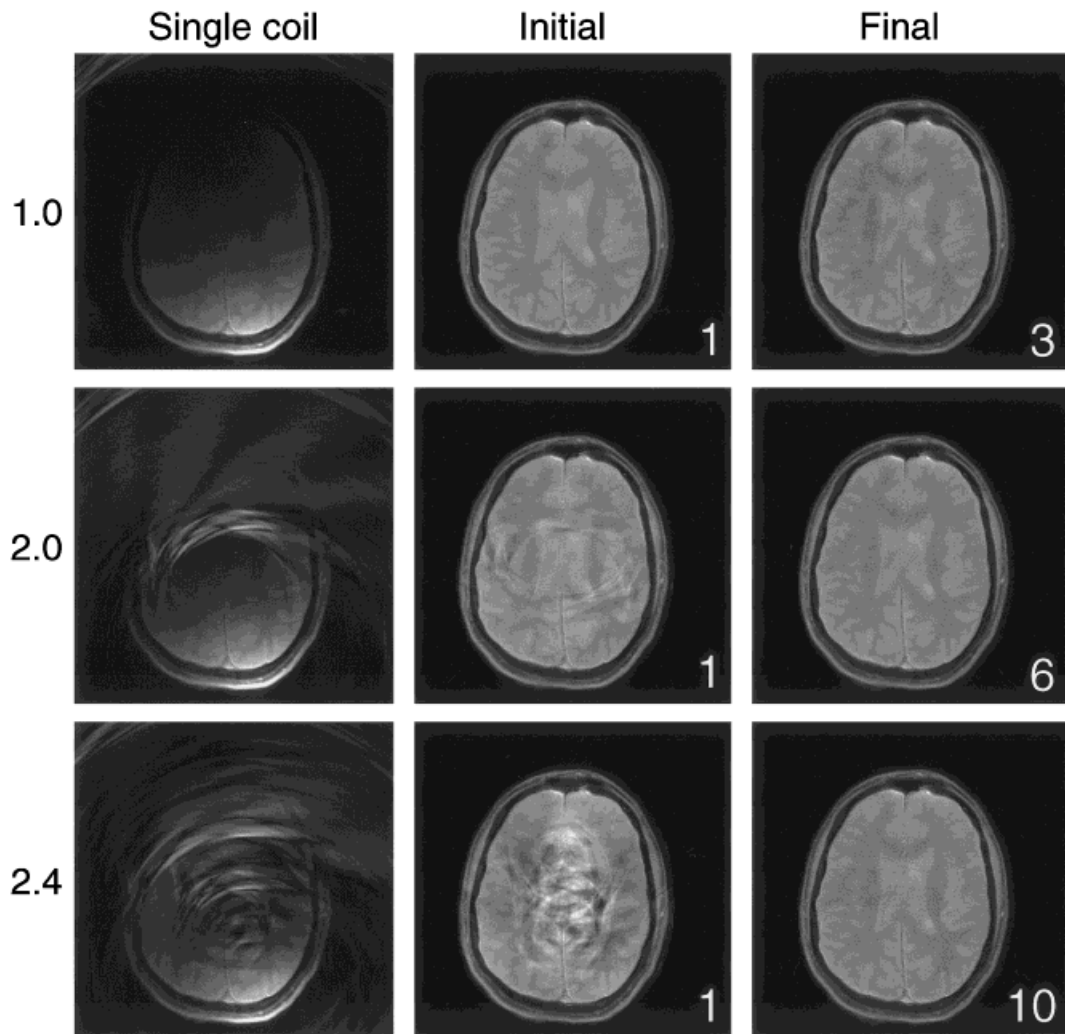


FIG. 5. Sensitivity-encoded brain imaging using six coils and spiral acquisition. The reduction factor was varied between  $R = 1.0$  (no reduction) and  $R = 6.0$ . The middle column shows the first approximation calculated in iterative reconstruction. The final results and iteration counts are shown on the right. For comparison, the left column shows images obtained with conventional reconstruction from single-coil data.

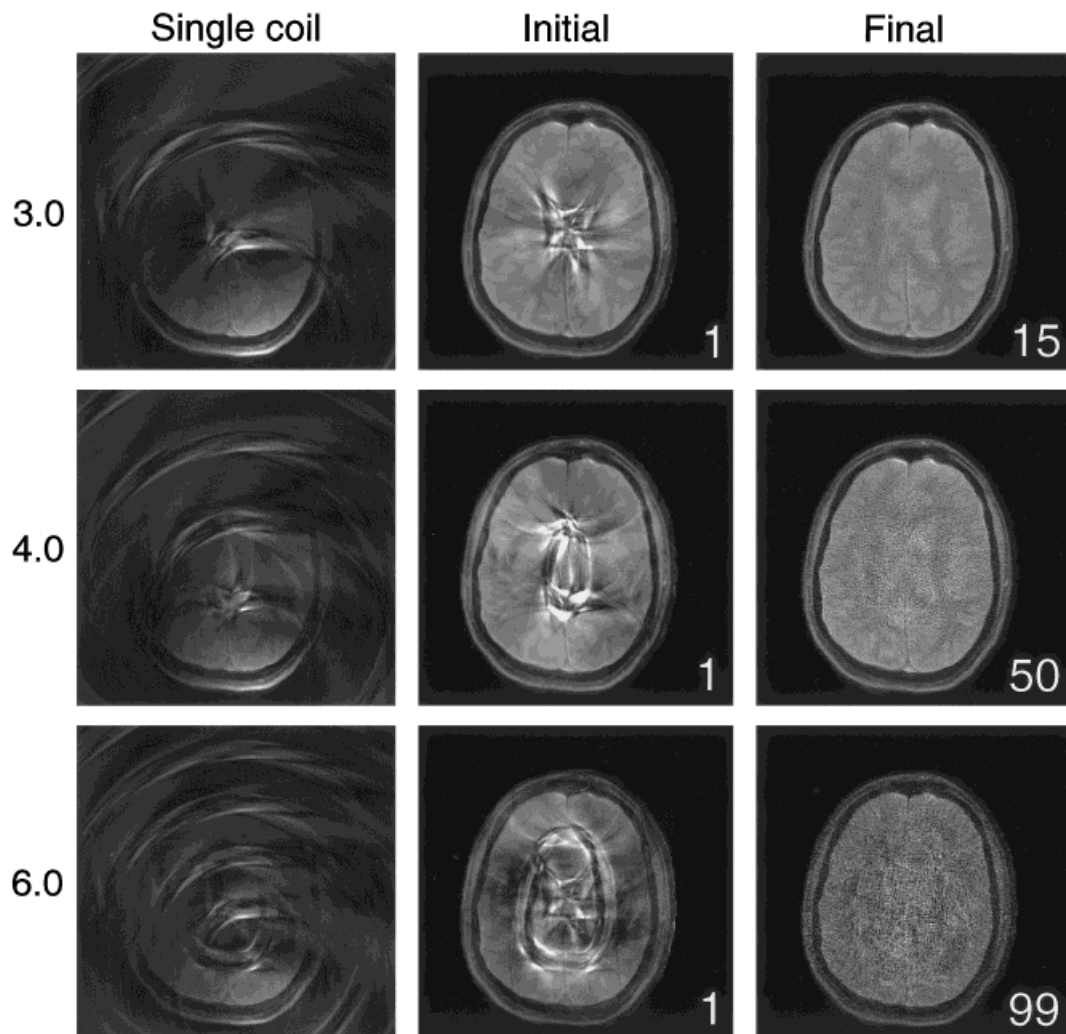


FIG. 5. Continued.

on the basis of an additional data set acquired with a body coil. Using the resulting maps, sensitivity-based reconstruction was performed for each subset of two interleaves. Six iterations were carried out per image, applying both density and intensity correction.

Samples of the resulting image series are displayed in Fig. 6. Four successive frames are shown together with the two conventional images which were reconstructed from the same data. Due to fast cardiac motion during data acquisition, the right coronary artery appears blurred in the first conventional image. Furthermore, this image exhibits slight, ring-shaped motion artifacts. In the sensitivity-encoded series with doubled frame-rate, the coronary vessel is more clearly depicted, resolving a slight counter-clockwise displacement. Furthermore, the motion artifact observed in the conventional images is not visible in the SENSE series. However, due to shorter acquisition and nonunitary reconstruction, the sensitivity-encoded images exhibit visibly enhanced noise.

## DISCUSSION

The proposed iterative method has been successfully applied for SENSE reconstruction from data obtained with

various types of  $k$ -space trajectories, including the practically important spiral and radial patterns. The suggested combination of the CG algorithm with forward and reverse gridding and FFT reduces the computation complexity of image generation drastically with respect to direct methods. In fact, each iteration step requires only about twice as many operations as conventional gridding reconstruction from multiple-coil data.

The still relatively long computation times reported in this work are mainly due to the nonoptimized preliminary software used. A rough estimation indicates that efficient implementation and fast computing hardware will reduce reconstruction time to a convenient range. Note that the most demanding operations in the proposed procedure, gridding and FFT, are carried out independently for each receiver channel. The algorithm is therefore perfectly suited for parallel computing with multiple CPUs. This option promises SENSE reconstruction from arbitrary  $k$ -space trajectories at rates similar to those typically accomplished in conventional gridding reconstruction. The immediate comparison of the proposed procedure with direct methods is limited to relatively small image matrices, where direct reconstruction is practical. Using a straightforward Gauss elimination scheme, the reconstruction of a

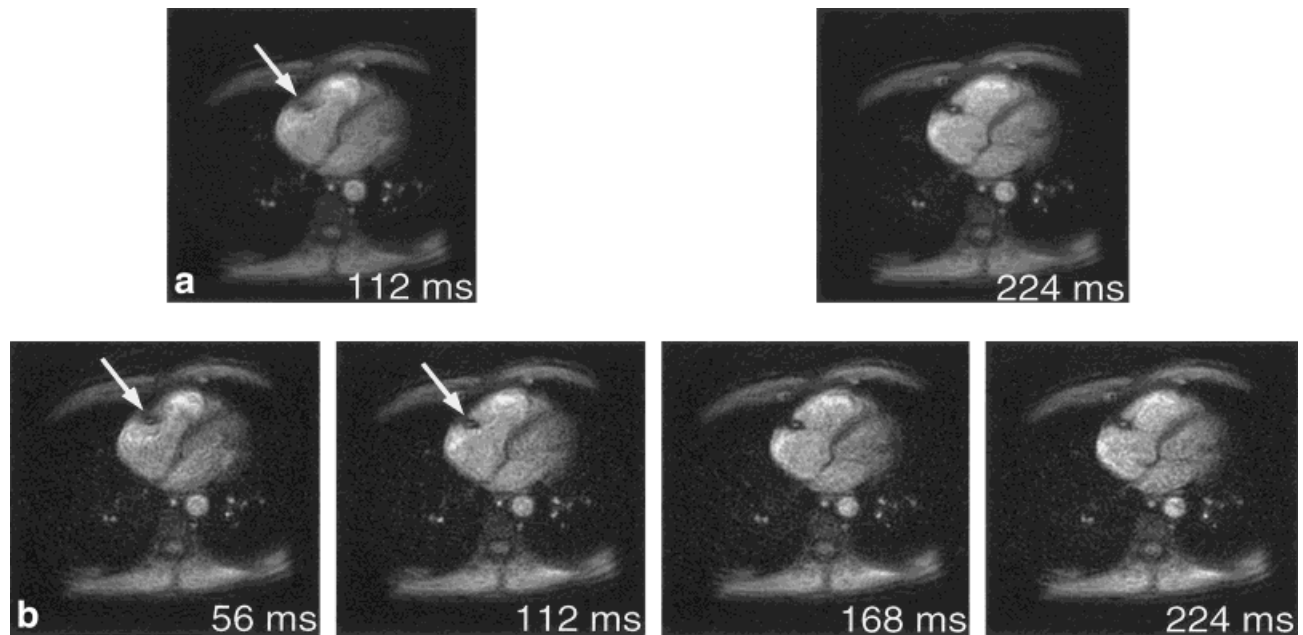


FIG. 6. Real-time cardiac imaging. Sensitivity-encoded heart imaging with four coils, using a real-time spiral protocol. **a**: Conventional reconstruction from fully-Fourier-encoded data obtained with four successive spiral interleaves. **b**: Images obtained from the same data by sensitivity-based reconstruction using only two successive interleaves for each image. In this fashion, the scan time per image was reduced from 112 ms to 56 ms.

$64 \times 64$  image, for example, takes more than 12 min (15), as opposed to 25 s at  $R = 2.5$ , as accomplished in the present work. At  $N = 128$ , the computational cost of direct methods exceeds that of the iterative method by orders of magnitude, as it grows at  $N^6$  as opposed to  $N^2 \log N$ .

The proposed algorithm is based on a general formula for SENSE reconstruction, which was previously derived theoretically in Ref. 6. It was found that this formula indeed yields intensity-corrected images free of residual aliasing, as required by the underlying voxel condition. In particular, by enforcing this condition, variations in the *k*-space sampling density are implicitly accounted for. Consequently, even with highly irregular random sampling a flawless image was obtained. Due to this ability, the algorithm may be useful also for conventional, fully-Fourier-encoded imaging with general trajectories. Its inherent density correction forms an interesting alternative to explicit density correction as usually performed in gridding methods (21).

It has been found that explicit correction for variations in sampling density and net coil sensitivity form valuable means of enhancing the convergence of the iteration process. The presented convergence study suggests several conclusions. For fast initial convergence, the combination of both types of correction seems most appropriate. In the reported experiments, too, this option was found to yield high accuracy after few iteration steps already. For most exact reconstruction with a large number of iterations, however, density correction alone seems more appropriate. On the other hand, intensity correction alone does not seem favorable for either purpose.

The convergence speed has also been found to strongly depend on the factor by which gradient encoding is reduced. Generally, convergence slows down as the reduc-

tion factor  $R$  increases. This behavior is related to the condition of the underlying linear system, which is a measure of the linear dependence of its component equations. In the CG method, just as in most other iterative numerical methods, the condition number is directly related to convergence speed. As the condition increases, convergence slows down. The observed behavior thus illustrates that the condition gradually deteriorates as the reduction factor grows.

Deteriorating condition is an adverse effect also with respect to image SNR. Irrespective of the numerical methods used for solving a linear system, its condition governs the influence of errors in input values on the solution of the system. High condition values indicate strong enhancement of input errors, particularly of noise. This effect was previously observed in SENSE imaging with Cartesian sampling patterns, where at high reduction factors deteriorating conditions resulted in adverse noise augmentation.

In this context it is important to note that in sensitivity-based reconstruction the calculation of each pixel value is individually conditioned, corresponding to individual sensitivity relations. Therefore, noise enhancement is a local effect, resulting in an inhomogeneous noise distribution in the final image. For the Cartesian case, this phenomenon has been quantitatively described by the so-called local geometry factor, which was derived by analysis of noise propagation (6). The same approach is valid also for non-Cartesian *k*-space sampling. The noise level in each pixel of the final image is given by the square-root of the corresponding diagonal entry of the image noise matrix  $X$  (Eq. [5]). However, as opposed to unfolding reconstruction in the Cartesian case, the iterative method proposed here does not yield image noise levels as a by-product. In



fact, the explicit calculation of final image noise is a more difficult task than image reconstruction alone in that  $X$  is a matrix and thus is not readily accessible by vector iteration. Nevertheless, the behavior of noise and SNR in sensitivity-based reconstruction is a key issue, requiring further investigation. In particular, SNR considerations govern the optimization of the coil arrangement and the range of reasonable reduction factors.

For SENSE reconstruction the encoding process is viewed as a general linear mapping rather than a pure FT. In principle, this approach permits incorporating a wide range of effects and disturbances occurring in MR experiments. For example, gradient delays and nonlinearity as well as  $B_0$  inhomogeneity may be accounted for by additional terms in the encoding matrix. However, by relying on FFT for efficient computation, the inversion algorithm proposed in this work is limited to encoding matrices which permit the separation of a pure Fourier part, as done in Eqs. [16] and [19]. For the treatment of  $B_0$  inhomogeneity, for example, the conventionally used segmentation approaches (27,28) may be incorporated in the forward and reverse gridding operations of the CG procedure.

## CONCLUSIONS

According to the results of this work, the proposed iteration scheme enables efficient image reconstruction from sensitivity-encoded data obtained with arbitrary  $k$ -space sampling patterns. The benefits of SENSE with coil arrays are thus made practically available in combination with all types of  $k$ -space trajectories. Enhanced imaging speed is of particular interest for spiral scanning with a range of promising applications, including real-time cardiac and coronary artery imaging and functional brain mapping.

## ACKNOWLEDGMENTS

The authors thank Stephan Kannengießer for exciting discussions.

## APPENDIX A

### Positive-Definiteness of $E^H \tilde{\Psi}^{-1} E$

According to Eqs. [B4] and [B7],  $\tilde{\Psi}$  has the Cholesky decomposition

$$\tilde{\Psi} = (L \otimes Id_{n_K})(L^H \otimes Id_{n_K}). \quad [A1]$$

Thus, assuming that  $E$  has maximal rank, for any vector  $\mathbf{x} \neq 0$

$$\mathbf{x}^H E^H \tilde{\Psi}^{-1} E \mathbf{x} = |(L^{-1} \otimes Id_{n_K}) E \mathbf{x}|^2 > 0, \quad [A2]$$

where  $|\cdot|$  denotes Euclidean length. Hence,  $E^H \tilde{\Psi}^{-1} E$  is positive definite. The same type of argument holds for  $IE^H DEI$  as  $I$  and  $D$  are real, diagonal matrices.

## APPENDIX B

### Noise Decorrelation by Cholesky Decomposition of $\Psi$

According to Eq. [8], the receiver noise matrix can be written as

$$\Psi = \frac{\hat{\eta} \hat{\eta}^H}{n_S}, \quad [B1]$$

where  $n_S$  denotes the number of noise samples taken per channel for noise assessment and

$$\hat{\eta}_{\gamma,\sigma} = \eta_{\gamma}(t_{\sigma}) \quad [B2]$$

lists these samples in an  $n_C \times n_S$  matrix,  $\gamma$  counting the coils and  $\sigma$  counting the samples. Thus, if  $\Psi$  is invertible, for any vector  $\mathbf{x} \neq 0$

$$\mathbf{x}^H \Psi \mathbf{x} = \left| \frac{\hat{\eta}^H \mathbf{x}}{\sqrt{n_S}} \right|^2 > 0 \quad [B3]$$

holds. Hence  $\Psi$  is positive-definite and allows the Cholesky decomposition

$$\Psi = LL^H, \quad [B4]$$

where  $L$  is an invertible, left-triangular matrix (20).

Creating virtual receiver channels by linear combination according to Eq. [10] results in the virtual set of noise samples

$$\hat{\eta}_{\gamma,\sigma}^{decorr} = \sum_{\gamma'} (L^{-1})_{\gamma,\gamma'} \hat{\eta}_{\gamma',\sigma} = [L^{-1} \hat{\eta}]_{\gamma,\sigma}. \quad [B5]$$

Hence the noise matrix of the virtual set of channels is given by

$$\Psi^{decorr} = \frac{\hat{\eta}^{decorr} (\hat{\eta}^{decorr})^H}{n_S} = L^{-1} \frac{\hat{\eta} \hat{\eta}^H}{n_S} (L^{-1})^H, \quad [B6]$$

which is equal to identity according to Eqs. [B1] and [B4]. Thus, the virtual channels exhibit unit variance noise without mutual correlation, and  $\Psi^{decorr}$  may be omitted. Equation [7] may be rewritten as

$$\tilde{\Psi} = \Psi \otimes Id_{n_K}, \quad [B7]$$

where  $Id_{n_K}$  denotes the  $n_K \times n_K$  identity matrix. Similarly, according to Eqs. [2] and [10]–[12], the transition to decorrelated channels may be rewritten as

$$E^{decorr} = (L^{-1} \otimes Id_{n_K}) E \quad [B8]$$

$$\mathbf{m}^{decorr} = (L^{-1} \otimes Id_{n_K}) \mathbf{m}. \quad [B9]$$

Hence, image reconstruction with decorrelated channels reads

$$\begin{aligned}
\mathbf{v} &= [(E^{decorr})^H E^{decorr}]^{-1} (E^{decorr})^H \mathbf{m}^{decorr} \\
&= [E^H [(L^{-1})^H L^{-1}] \otimes Id_{n_k} E]^{-1} E^H [(L^{-1})^H L^{-1}] \otimes Id_{n_k} \mathbf{m} \\
&= [E^H \tilde{\Psi}^{-1} E]^{-1} E^H \tilde{\Psi}^{-1} \mathbf{m}.
\end{aligned} \tag{B10}$$

Thus the solution  $\mathbf{v}$  obtained with decorrelation is identical to that of the original Eq. [4].

## APPENDIX C

Conjugate gradient (CG) iteration (adapted from Stoer and Bulirsch (29)), with a convergence check based on the  $\delta$ -criterion:

$\epsilon = \text{required accuracy}$   
 $\mathbf{b}_{approx}^{(0)} = \mathbf{0}$   
 $\mathbf{p} = \mathbf{a}$   
 $\mathbf{r}^{(0)} = \mathbf{a}$   
For  $i = 0, 1, \dots$  {  
 $\mathbf{r}^{(i)H} \mathbf{r}^{(i)}$   
 $\delta = \frac{\mathbf{a}^H \mathbf{a}}{\mathbf{a}^H \mathbf{a}}$   
If  $\delta < \epsilon$  then output  $\mathbf{b}_{approx}^{(i)}$ , stop  
Else {  
 $\mathbf{q} = IE^H DE \mathbf{p}$   
 $\mathbf{b}_{approx}^{(i+1)} = \mathbf{b}_{approx}^{(i)} + \frac{\mathbf{r}^{(i)H} \mathbf{r}^{(i)}}{\mathbf{p}^H \mathbf{q}} \mathbf{p}$   
 $\mathbf{r}^{(i+1)} = \mathbf{r}^{(i)} - \frac{\mathbf{r}^{(i)H} \mathbf{r}^{(i)}}{\mathbf{p}^H \mathbf{q}} \mathbf{q}$   
 $\mathbf{p} = \mathbf{r}^{(i+1)} + \frac{\mathbf{r}^{(i+1)H} \mathbf{r}^{(i+1)}}{\mathbf{r}^{(i)H} \mathbf{r}^{(i)}} \mathbf{p}$   
}  
}  
}

## REFERENCES

- Hutchinson M, Raff U. Fast MRI data acquisition using multiple detectors. *Magn Reson Med* 1988;6:87–91.
- Kelton JR, Magin RL, Wright SM. An algorithm for rapid image acquisition using multiple receiver coils. In: *Proceedings of the 8th Annual Meeting of SMRM, Amsterdam*, 1989. p 1172.
- Kwiat D, Einar S. A decoupled coil detector array for fast image acquisition in magnetic resonance imaging. *Med Phys* 1991;18:251–265.
- Ra JB, Rim CY. Fast imaging method using multiple receiver coils with subencoding data set. In: *Proceedings of the 10th Annual Meeting of SMRM, San Francisco*, 1991. p 1240.
- Sodickson DK, Manning WJ. Simultaneous acquisition of spatial harmonics (SMASH): ultra-fast imaging with radiofrequency coil arrays. *Magn Reson Med* 1997;38:591–603.
- Pruessmann KP, Weiger M, Scheidegger MB, Boesiger P. SENSE: sensitivity encoding for fast MRI. *Magn Reson Med* 1999;42:952–962.
- Griswold MA, Jakob PM, Nittka M, Goldfarb JW, Haase A. Partially parallel imaging with localized sensitivities (PILS). In: *Proceedings of the 8th Annual Meeting of ISMRM, Denver*, 2000. p 273.
- Kyriakos WE, Panych LP, Kacher DF, Westin CF, Bao SM, Mulken RV, Jolesz FA. Sensitivity profiles from an array of coils for encoding and reconstruction in parallel (SPACE RIP). *Magn Reson Med* 2000;44:301–308.
- Ahn BC, Kim JH, Cho ZH. High-speed spiral-scan echo planar NMR imaging. *IEEE Trans Med Imaging* 1986;MI-5:2–7.
- Meyer CH, Hu BS, Nishimura DG, Macovski A. Fast spiral coronary artery imaging. *Magn Reson Med* 1992;28:202–213.
- Lauterbur PC. Image formation by induced local interactions: examples employing nuclear magnetic resonance. *Nature (Lond)* 1973;242:190–191.
- Glover GH, Noll DC. Consistent projection reconstruction (CPR) techniques for MRI. *Magn Reson Med* 1996;29:345–351.
- Scheffler K, Hennig J. Frequency resolved single-shot MR imaging using stochastic k-space trajectories. *Magn Reson Med* 1996;35:569–576.
- Lauzon ML, Rutt BK. Effects of polar sampling in k-space. *Magn Reson Med* 1996;36:940–949.
- Pruessmann KP, Weiger M, Boernert P, Boesiger P. Spiral SENSE: sensitivity encoding with arbitrary k-space trajectories. In: *Proceedings of the 7th Annual Meeting of ISMRM, Philadelphia*, 1999. p 94.
- Pruessmann KP, Weiger M, Boernert P, Boesiger P. A gridding approach for sensitivity encoding with arbitrary trajectories. In: *Proceedings of the 8th Annual Meeting of ISMRM, Denver*, 2000. p 276.
- Kannengießer SAR, Brenner AR, Noll TG. Accelerated image reconstruction for sensitivity encoded imaging with arbitrary k-space trajectories. In: *Proceedings of the 8th Annual Meeting of ISMRM, Denver*, 2000. p 155.
- Hestenes MR, Stiefel E. Methods of conjugate gradients for solving linear systems. *Natl Bur Standards J Res* 1952;49:409–436.
- Stoer J, Bulirsch R. *Numerische Mathematik* 2, 3rd ed. Heidelberg: Springer; 1990. p 301.
- Stoer J. *Numerische Mathematik* 1, 5th ed. Heidelberg: Springer; 1989. p 163.
- Jackson JI, Meyer CH, Nishimura DG, Macovski A. Selection of a convolution function for Fourier inversion using gridding. *IEEE Trans Med Imaging* 1991;MI-10:473–478.
- Roemer PB, Edelstein WA, Hayes CE, Souza SP, Mueller OM. The NMR phased array. *Magn Reson Med* 1990;16:192–225.
- Rasche V, Proksa R, Sinkus R, Bönnert P, Eggers H. Resampling of data between arbitrary grids using convolution interpolation. *IEEE Trans Med Imaging* 1999;18:385–392.
- Weiger M, Pruessmann KP, Leussler C, Roschmann P, Boesiger P. Specific coil design for SENSE: a six-element cardiac array. *Magn Reson Med* 2001;45:495–504.
- Börnert P, Schomberg H, Aldefeld B, Groen J. Improvements in spiral MR imaging. *MAGMA* 1999;9:29–41.
- Weiger M, Pruessmann KP, Boesiger P. Cardiac real-time imaging using SENSE. *Magn Reson Med* 2000;43:177–184.
- Noll DC, Meyer CH, Pauly JM, Nishimura DG, Macovski A. A homogeneity correction method for magnetic resonance imaging with time-varying gradients. *IEEE Trans Med Imaging* 1991;10:629–637.
- Man LC, Pauly JM, Macovski A. Multifrequency interpolation for fast off-resonance correction. *Magn Reson Med* 1997;37:785–792.
- Stoer J, Bulirsch R. *Numerische Mathematik* 2, 3rd ed. Heidelberg: Springer; 1990. p 296.